PT Symmetry and Singularity-Enhanced Sensing Based on Photoexcited Graphene Metasurfaces

Pai-Yen Chen and Jeil Jung

Phys. Rev. Applied **5**, 064018 — Published 29 June 2016

DOI: 10.1103/PhysRevApplied.5.064018

$\mathcal{PT}$-Symmetry and Singularity-Enhanced Sensing Based on Photoexcited Graphene Metasurfaces

Pai-Yen Chen[1,*] *and Jeil Jung*[2]

[1]Department of Electrical and Computer Engineering, Wayne State University, Detroit, MI 48017, U.S.A.

[2]Department of Physics, University of Seoul, Seoul, 130-743, Korea

RECEIVED DATE

Corresponding Author: Email: pychen@wayne.edu

ABSTRACT: We introduce here a parity-time ($\mathcal{PT}$) symmetric system using an optically-pumped, active graphene metasurface paired with a resistive metallic filament, realizing a unidirectional reflectionless propagation of terahertz (THz) waves. The amplified THz stimulated emission and tailored plasmon resonances in the graphene metasurface may achieve an equivalent negative-resistance converter at THz frequencies. We theoretically demonstrate that the combination of the spectral singularity in a $\mathcal{PT}$-symmetric system and the chemical sensitivity of graphene may give rise to exotic scattering responses, strongly influenced by the presence of charged impurities in graphene at the spontaneous $\mathcal{PT}$-symmetry breaking point. This graphene-based $\mathcal{PT}$-symmetric device may have broad relevance beyond the extraordinary manipulation of THz waves, as it may also

open exciting prospects for detecting gas, chemical, and biological agents with high sensitivities.

KEYWORDS: Parity-time symmetry, graphene, terahertz waves, metasurfaces, graphene sensors

I. INTRODUCTION

In the past decade, significant attention has been devoted to parity-time ($\mathcal{PT}$) symmetric quantum Hamiltonian systems [1]-[6], since it was shown that even non-Hermitian Hamiltonians can exhibit entirely real eigenspectra, provided that the system is invariant under combined operations of parity ($\mathcal{P}$) and time-reversal ($\mathcal{T}$) symmetry [1]-[3]. The linear operator $\mathcal{P}$ performs the spatial inversion that transforms coordinates and momenta, whereas the antilinear operator $\mathcal{T}$ conducts the time inversion. The simultaneous application of both operators $\mathcal{PT}$ is antilinear, implying that the quantum potential must satisfy the specific condition $V(x) = V^*(-x)$. [1]-[3] Considering the antilinear character of the $\mathcal{PT}$ operator, the Hamiltonian and $\mathcal{PT}$ operator do not always share the same eigenvectors. Beyond some non-Hermiticity threshold, typically referred to as the spontaneous $\mathcal{PT}$-symmetry breaking point or the exceptional point, an abrupt phase transition may occur and the eigenspectrum becomes complex. The existence of this degeneracy point in non-Hermitian systems exhibits an interesting property that both the eigenvalues and the eigenvectors simultaneously converge [1]-[6].

Although the concept of $\mathcal{PT}$-symmetric quantum systems is still under intensive debate [7], its optics [4]-[6],[8]-[27] and acoustic [28],[29] analogues have been recently explored, by exploiting the formal similarities between the Schrödinger and Helmholtz equations. Optics emerges as the most versatile platform for exploring $\mathcal{PT}$-symmetric physics, since it is technologically viable with spatially-modulated distributions of optical gain and loss [11],[16],[17],[25]. During recent years, several $\mathcal{PT}$-symmetric applications have been discovered in the optical domain, including the unidirectional propagation phenomena (e.g., unidirectional invisibility and negative refraction) [4]-[6],[8]-[27], planar focusing [23], beam switching [30],[31], coherent perfect laser absorbers [9],[15], and optical isolators and circulators [12],[20],[25],[26], which find diverse potential applications in photonic devices and systems.

In this work, we propose the concept and a realistic design of a $\mathcal{PT}$-symmetric system in the THz regime, as shown in Fig. 1(a), which properly balances loss and gain using a resistive metallic filament and an optically-pumped, amplifying graphene metasurface. These two absorbing and gain thin sheets, separated by an air or dielectric gap with thickness *d*, are characterized by a $\mathcal{PT}$-symmetric impedance distribution $Z_T = -Z_B$, where *T* and *B* represent the top and bottom interfaces. At THz frequencies, an optically-pumped graphene metasurface may exhibit a negative surface resistance $Z_T = -R$, opposite to that of metallic filament $Z_B = R$, thanks to the population inversion produced by cascaded optical photon emissions [32]-[37]. Such a paired absorbing and amplifying impedance

sheets may effectively realize the simplest possible $\mathcal{PT}$-symmetric system [23], which supports the unidirectional transparency for THz waves. Furthermore, we propose for the first time that the unusual scattering properties around the singular frequency (exceptional point) may have potential to realize ultrasensitive chemical, molecular, and biological sensing, as illustrated in Fig. 1(b). It is based on unique properties of graphene in the THz regime that the dynamic conductivity of graphene can be varied by surface dopants (e.g. reactive gas/molecular/chemical species), chemically modulating the surface impedance of graphene metasurface. This surface-impedance perturbation results in dramatically altered scattering properties of a $\mathcal{PT}$-symmetric metasurface, associated with the eigenvalue bifurcation of the scattering matrix. As we show below, a $\mathcal{PT}$-symmetric reflection-type sensor can potentially have much higher sensitivity compared to conventional passive, graphene-based plasmonic sensors.

II. PT-SYMMETRY-INDUCED SCATTERING PROPERTIES

As illustrated in Fig. 1, the geometry of interest features a $\mathcal{PT}$-symmetric THz system composed of two isotropic, homogeneous surface impedances Z_T and Z_B, which can be modeled using an equivalent two-port transmission-line network model in Fig. 2. We assume here that graphene and metal filament are suspended in air, being the same as the outside medium, and that a transverse-magnetic (TM)-polarized terahertz wave is normally incident on the impedance sheets [Fig. 1(a)]; the terahertz wave is propagating along the z-axis, with the electric field vector polarized in a direction perpendicular to the graphene-

nanoribbons (y-axis). In this case, the deeply-subwavelength metallic filament and graphene can be represented as two parallel lumped elements, separated by a transmission-line segment of electrical length $x=k_0 d$, characteristic impedance $Z_0 = \sqrt{\mu_0 / \varepsilon_0}$, and propagation constant $k_0 = \omega\sqrt{\mu_0 \varepsilon_0}$. Specifically, we employ the metasurface structure [Fig. 2(a)] to support enhanced light-matter interactions in graphene, and to balance the kinetic inductance of graphene with the geometric capacitance of metasurface; hence, no reactive power is being stored around the graphene surface. This leads to a purely real and negative surface impedance $Z_T = -R = -\kappa Z_0$, where κ is the dimensionless non-Hermiticity parameter $\{\kappa \in \mathrm{R} : \kappa \geq 0\}$. The thickness-dependent surface resistance of a metallic filament is always positive ($Z_B = +R = \kappa Z_0$) in the THz range [38]. Using the transfer-matrix method [39],[40] (see Appendix A for details) and assuming a time-harmonic field of the form $e^{j\omega t}$, the scattering matrix $\mathbf{S}$ of the system in Fig. 2 can be derived as:

$$\mathbf{S} = \begin{pmatrix} t & r_T \\ r_B & t \end{pmatrix} = \begin{pmatrix} \dfrac{1}{e^{jx} - j\sin(x)/(2\kappa^2)} & \dfrac{(1+2\kappa)\sin(x)}{-\sin(x) - 2j\kappa^2 e^{jx}} \\ \dfrac{(1-2\kappa)\sin(x)}{-\sin(x) - 2j\kappa^2 e^{jx}} & \dfrac{1}{e^{jx} - j\sin(x)/(2\kappa^2)} \end{pmatrix} \qquad (1)$$

, where r_T and r_B are the reflection coefficients for THz waves incident from the top and bottom, respectively, and t is the transmission coefficient, which is independent of the direction of incidence. It can be straightforwardly demonstrated that the scattering matrix in Eq. (1) indeed follows the special symmetry: $\mathcal{PT}\,\mathbf{S}^*(\omega)\mathcal{PT} = \mathbf{S}^{-1}(\omega)$, as typical of a $\mathcal{PT}$-symmetric system [14].

Figure 2(a) shows the loci of complex scattering coefficients on a polar diagram for $x = \sin^{-1}(1/4)$, as the parameter κ is varied; each color in the legend represents different normalized resistance values. It is seen that the top reflection r_T can, in principle, differ from the bottom reflection r_B. A condition of special interest resides in the exceptional point occurring when κ = 0.5. At such frequency, one can obtain the unidirectional transparency with zero and unitary reflection for light incident from the bottom and top ($|r_B| = 0$ and $|r_T| = 0$), while with an unitary transmission for both sides ($|t| = 1$). This unidirectional reflectionless property is rather independent of the separation distance *d*. For instance, the scattering matrix for κ = 0.5 and arbitrary *x* becomes:

$$\mathbf{S} = \begin{pmatrix} e^{jx} & -2 + 2e^{2jx} \\ 0 & e^{jx} \end{pmatrix}, \tag{2}$$

which clearly shows that the reflectionless perfect transmission occurs in one direction but not the other. The product of two reflections in Eq. (2) is zero, as the nature of $\mathcal{PT}$-symmetric systems leads to $r_B r_T^* = 1 - |t|^2$. [14] In Fig. 2(a), the change of the transmission coefficient from $|t| < 1$ to $|t| > 1$ is associated with the transition from the $\mathcal{PT}$-symmetric phase to the $\mathcal{PT}$-broken phase. At the exceptional point, achievable with $\kappa = 0.5$ and $x = \sin^{-1}(1/4)$, the unidirectional reflectionless propagation with perfect transmission and unitary top reflection can be achieved.

In one-dimension systems, the transition between the $\mathcal{PT}$ symmetry and symmetry-breaking can be identified by tracing the behavior of eigenvalues of the scattering matrix $\mathbf{S}$ [14]. The eigenvalues of $\mathbf{S}$ in Eq. (1) can be derived as:

$$\lambda_{\pm} = \frac{2\kappa^2 \pm \sqrt{(4\kappa^2 - 1)\sin^2(x)}}{2\kappa^2 e^{jx} - j\sin(x)}. \tag{3}$$

In the $\mathcal{PT}$-symmetric phase, the two eigenvalues are nondegenerate and unimodular ($|\lambda_{\pm}|=1$), whereas the non-unimodular eigenvalues ($\lambda_{+} = 1/(\lambda_{-})^{*}$) suggest the $\mathcal{PT}$-broken phase. From Eq. (3), we find that regardless of x, when $\kappa > 0.5$, the unimodular eigenvalues ($\lambda_{\pm}$) would transit to non-unimodular ones. At the exceptional point, the scattering matrix eignevalues are equal ($\lambda_{+} = \lambda_{-} = 1/(\lambda_{+})^{*}$). Figure 2(b) presents the complex eigenvalues of $\mathbf{S}$ as a function of the parameter κ, showing that the eigenvalues are unimodular and nondegenerate for $\kappa < 0.5$ ($\mathcal{PT}$-symmetric phase with $|t|<1$) and have reciprocal moduli for $\kappa > 0.5$ ($\mathcal{PT}$-broken phase with $|t|>1$), consistent with the evolution of transmission coefficient in Fig. 2(a). We also note that a directional transparency can be obtained when $x = n\pi$, leading to $r_B = r_T^{*} = 0$, $t = e^{-jn\pi}$, and $\lambda = 1$ or -1, in some sense similar to a resonant loss-gain compensation medium.

III ACTIVE GRAPHENE METASURFACES

Graphene, as a single layer hexagonal network of carbon atoms, is of great interest as a novel material for integrated photonics and optoelectronics, since it can exhibit strong optical absorption, up to 2.3% for a single atomic layer [41],[42] and ultrafast modulation of its conductivity by electrostatic gating in the terahertz

to mid-infrared regimes [43]-[51]. The non-equilibrium terahertz properties of graphene are especially interesting because the population inversion and negative dynamic conductivity (THz gain) can take place in an optically-pumped graphene monolayer, due to the cascaded optical-phonon emission and interband transitions around the Dirac point [32]-[37], as illustrated in Fig. 3(a). The photoexcited electron-hole pairs in graphene splits the Fermi level into two quasi-Fermi levels $E_{Fn}, E_{Fp} = \pm\varepsilon_{\mathrm{F}}$ that respectively define the electron and hole concentrations. Since the relaxation time for intraband transitions is of the order of $\tau \approx 1$ ps, which is faster than the recombination time $\tau \approx 1$ ns for electron-hole pairs [52], the population inversion can be achieved with the optical pumping [32]-[37]. Under the sufficiently strong optical excitation, the interband emission of photons may prevail over the intraband Drude absorption, and thus the real part of the dynamic conductivity of graphene $\mathrm{Re}[\sigma]$ can be negative. Due to the unique gapless energy spectra of electrons and holes in graphene, the negative $\mathrm{Re}[\sigma]$ can occur at relatively low frequencies, such as the THz spectral range. The dynamic conductivity of graphene modeled from non-equilibrium Green's functions [46], comprising the contributions of both interband and intraband transitions, i.e. $\sigma = \sigma_{\mathrm{intra}} + \sigma_{\mathrm{inter}}$, given by:

$$\sigma_{\mathrm{intra}} = j\frac{q^2}{\pi\hbar^2}\frac{1}{\omega - j\tau^{-1}}\left[\int_0^\infty \varepsilon\left(\frac{\partial F_1(\varepsilon)}{\partial\varepsilon} - \frac{\partial F_2(-\varepsilon)}{\partial\varepsilon}\right)d\varepsilon\right] \tag{4a}$$

$$\sigma_{\mathrm{inter}} = -j\frac{q^2}{\pi\hbar^2}(\omega - j\tau^{-1})\int_0^\infty \frac{F_2(-\varepsilon) - F_1(\varepsilon)}{(\omega - j\tau^{-1})^2 - 4\varepsilon^2/\hbar^2}d\varepsilon, \tag{4b}$$

where $F_1(\varepsilon)=\left[1+e^{(\varepsilon-E_{Fn})/K_BT}\right]^{-1}$, $F_2(\varepsilon)=\left[1+e^{(\varepsilon-E_{Fp})/K_BT}\right]^{-1}$, q is the electric charge, □ the is the energy, $\hbar$ is the reduce Planck's constant, K_B is the Boltzmann's constant, T is the temperature, ω is the angular frequency, and τ is the momentum relaxation time of charge carriers (here we assume τ = 1 ps, which is consistent with experimental results [52]). By solving the integral in Eq. 4(a), σ_{intra} can be written in a compact form:

$$\sigma_{intra}=\left(\frac{q^2}{4\hbar}\right)\left(\frac{8k_BT}{\pi\hbar}\ln\left[1+e^{\varepsilon_F/k_BT}\right]\right)\left(\frac{\tau}{1+\omega^2\tau^2}-j\frac{\omega}{\omega^2+\tau^{-2}}\right). \quad (5)$$

$\mathrm{Re}[\sigma_{inter}]$ in Eq. 4(b) could be negative, which, however, must compete with the positive $\mathrm{Re}[\sigma_{intra}]$ in Eq. (5). For instance, in the THz spectral range, $\mathrm{Re}[\sigma_{inter}]$ can be approximately expressed as [32]:

$$\mathrm{Re}[\sigma_{inter}]\approx\frac{q^2}{4\hbar}\tanh\left(\frac{\hbar\omega-2\varepsilon_F}{4K_BT}\right), \quad (6)$$

which can be negative if $\hbar\omega<2\varepsilon_F$. Figure 3(b) shows $\mathrm{Re}[\sigma]$ as a function of frequency for a graphene monolayer with ε_F = 25 meV at different temperatures; here the equilibrium conductivities (without optical excitation and E_F = ε_F) are also presented for comparison. It is seen that under the optical excitation, Re[σ] can be negative even at room temperature, implying that THz amplification may be realized over a single layer of atoms. This property is crucial for making $\mathcal{PT}$-symmetry systems with balanced gain and loss. In the following, we assume a low

operating temperature T = 3 K. Figure 3(c) shows $\mathrm{Re}[\sigma]$ (solid lines) and $\mathrm{Im}[\sigma]$ (dashed lines) as a function of frequency for graphene with different quasi-Fermi energies; here dots represent the equilibrium $\mathrm{Re}[\sigma]$ with Fermi energy $E_\mathrm{F} = \varepsilon_\mathrm{F}$. The THz gain bandwidth is related to the energy splitting of quasi-Fermi levels, primarily controlled by the intensity of photodoping pump source (see Appendix B for details). The equilibrium and nonequilibrium conductivities would converge to a similar form in low-frequency (e.g. microwaves) and high-frequency (e.g. mid-infrared) regimes. In the visible and near-infrared spectral ranges, where the photon energy $\hbar\Omega_0 >> \varepsilon_\mathrm{F}, K_\mathrm{B}T,$ only the interband contribution is important and the optical conductivity becomes:

$$\sigma = \frac{q^2}{4\hbar}\tanh\left(\frac{\hbar\Omega_0 - 2\varepsilon_F}{4K_\mathrm{B}T}\right) \approx \frac{q^2}{4\hbar}. \tag{7}$$

We note here that the magnitude of $\mathrm{Re}[\sigma]$ is bounded by the physical limit of $\pm q^2/4\hbar$, as can be understood from Eqs. (5)-(7). From Fig. 3(c), it is also seen that graphene has a large kinetic inductance in the THz regime ($\mathrm{Im}[\sigma] < 0$). In order to satisfy the $\mathcal{PT}$-symmetric conditions [Eq. (2)], the inductive nature of graphene must be suppressed by conjugate capacitive elements, which, for instance, can be achieved with the graphene-nanoribbon metasurface in Fig. 1(a). If a graphene nanoribbon array has a subwavelength period, its equivalent surface impedance for the normally incident transverse-magnetic (TM) plane wave can be expressed as (see Appendix C for generalized expressions) [53]-[56]:

$$Z_s = R_s + jX_s = \frac{1}{\sigma(1-\varphi)} - j\frac{Z_0}{\psi \ln\left[\csc(\pi\varphi/2)\right]}$$
$$= \frac{1}{(1-\varphi)}\frac{\mathrm{Re}[\sigma]}{|\sigma|^2} - j\left\{\frac{1}{(1-\varphi)}\frac{\mathrm{Im}[\sigma]}{|\sigma|^2} + \frac{Z_0}{\psi \ln\left[\csc(\pi\varphi/2)\right]}\right\} \quad (8)$$

where $\sigma(\omega)$ is the conductivity of graphene monolayer, φ represents the ratio between the gap g and period a of the graphene-nanoribbon array [Fig. 1(a)], $\psi(\omega) = 2\omega a/\pi c = 4a/\lambda$, c is the speed of light, and λ is the wavelength. The second term in (8) accounts for the net contribution of the kinetic inductance per unit cell $L_K = \mathrm{Im}[\sigma]/\omega(1-\varphi)|\sigma|^2$ [57] and the geometric capacitance per unit cell $C_{ES} = \varepsilon_0 2a \ln\left[\csc(\pi\varphi/2)\right]/\pi$, [58]-[60] which are in series with the resistance per unit cell $R_s = \mathrm{Re}[\sigma]/(1-\varphi)|\sigma|^2$ as $Z_s = R_s + j(\omega L_K - 1/\omega C_{ES})$. We propose here a design approach to determine the optimal set of dimensionless parameters φ and ψ, which achieve the conditions $\mathrm{Re}[Z_s] = -Z_0/2$ and $\mathrm{Im}[Z_s] = 0$, necessary for obtaining the $\mathcal{PT}$-symmetry-induced unidirectional reflectionless effect. First, given the nonequilibrium conductivity of graphene at the frequency $\omega_0/2\pi$, the optimal value of φ that achieves $\mathrm{Re}[Z_s(\omega_0)] = -Z_0/2$ can be obtained from first term of Eq. (8) as:

$$\varphi_0 = 1 + \frac{2Z_0\,\mathrm{Re}[\sigma(\omega_0)]}{|\sigma(\omega_0)|^2} \quad (9)$$

Then, by applying φ_0 to the second term of Eq. (8), the optimal value of ψ that makes $\mathrm{Im}[Z_s(\omega_0)] = 0$ can be obtained as:

$$\psi_0 = -\frac{(1-\varphi_0)\,|\sigma(\omega_0)|^2\, Z_0}{\mathrm{Im}[\sigma(\omega_0)]\ln\left[\csc(\pi\varphi_0/2)\right]}. \qquad (10)$$

As a result, a photoexcited graphene-nanoribbon metasurface with physical parameters $d = \varphi_0 a$ and $a = \psi_0 \pi c / 2\omega_0$ may have a purely real and negative surface impedance $Z_s = -Z_0/2$ at the design frequency $\omega_0/2\pi$.

Figure 4(a) shows the frequency dispersion of surface resistance (solid lines) and surface reactance (dashed lines) for photoexcited graphene sheets ($\varepsilon_F = 15$ meV) of different configurations: (i) uniform graphene monolayer (blue lines) and (ii) graphene-nanoribbon metasurface with $(\varphi_0, \psi_0) = (0.164, 0.08)$ (red lines); here a metasurface made of conducting metal of the same dimensions is also presented for comparison (black lines). As can be seen in Fig. 4(a), it is possible to achieve zero reactance by balancing the intrinsic kinetic inductance of graphene with the geometric capacitance of nanoribbons. Therefore, a single metasurface can exhibit a highly controllable capacitive or inductive response, very different, and more appealing, than conventional metallic metasurfaces that are essentially capacitive at THz frequencies. On the other hand, a graphene monolayer always displays an inductive surface reactance with $\mathrm{Im}[Z_s] > 0$. Figure 4(b) shows a zoom-in of Fig. 4(a) around the design frequency $\omega_0/2\pi$ (here $\omega_0/2\pi$ = 1.5 THz). A graphene metasurface with geometric parameters (φ_0, ψ_0) displays a negative surface resistance of $-Z_0/2$ and a zero surface reactance, consistent with the conditions for the $\mathcal{PT}$-symmetry-induced unidirectional transparency.

The resistive portion (loss) of a $\mathcal{PT}$-symmetric system can be readily achieved with a metallic filament that is separated from the amplifying graphene metasurface by a distance $x = \sin^{-1}(1/4)$. The surface resistance of an ultrathin metal filament of thickness t_m can be expressed as $R_s = 1/(\sigma_m t_m)$, where the Drude conductivity $\sigma_m(\omega) = \sigma_0/(1 + j\omega\tau) \approx \sigma_0$ (the relaxation time τ for common metals are on the order of 10^{-14} s [38]). For instance, a nichrome (NiCr) filament with $\sigma_m = 6.7\times10^5$ [S/m] [38] and t_m = 7.9 nm displays a surface resistance of $+Z_0/2$ over a broad THz range.

IV. PT-SYMMETRIC TERAHERTZ SYSTEMS AND SENSOR APPLICATIONS

Here, we consider the realistic gain and loss properties of the optically-pumped graphene metasurface (denoted as GMTS 1) in Fig. 4 and a 7.9-nm-thick nichrome filament, forming the $\mathcal{PT}$-symmetric THz system in Fig. 1(a) at the design frequency $\omega_0/2\pi$ =1.5 THz. The vacuum gap size is 8.04 μm, which satisfies the condition of exceptional point: $x = \sin^{-1}(1/4)$ at 1.5 THz. Figure 5(a) shows the calculated reflectance and transmittance against frequency for this $\mathcal{PT}$-symmetric system. Figure 5(b) is similar to Fig. 5(a), but for the phase variations in the frequency response. It is seen that the system is unidirectionally transparent, with $|t|^2 = 1, |r_T|^2 = 1,$ and $|r_B|^2 = 0,$ at the exceptional point. At that frequency, the phase of r_B experiences an abrupt change of π, which is related to the singularity of zero reflection at the bottom interface, as the consequence of the onset of a

spontaneous $\mathcal{PT}$-symmetry breaking [14]. In addition, due to the step-function-like behavior of the phase, the delay time $\tau_{\text{delay}} = \partial \arg(r_B) / \partial \omega$ behaves as a delta function, implying that the reflected waves are trapped for a long time and being completely absorbed by the resistive sheet. Figures 5(a) and 5(b) also show a $\mathcal{PT}$-symmetric device designed to show an exceptional point at 1.8 THz. We find that the exceptional point and the associated unidirectional transparency can be upshifted to 1.8 GHz by using a graphene metasurface (denoted as GMTS 2) with $\varepsilon_F = 20$ meV and geometric parameters $(\varphi_0, \psi_0) = (0.23,\ 0.11)$; these values are calculated based on Eqs. (9) and (10). We should note that passive metasurfaces, if properly designed and implemented into the non-Hermitian system, may also achieve the unidirectional reflection at the exceptional points [61]. Nonetheless, the unidirectional transparency, with perfect transmissions and strongly asymmetric reflections, can only occur in the $\mathcal{PT}$-symmetric system involving a gain medium.

In recent years, sensing applications using graphene have been intensively studied, since its low density of states renders static/dynamic electrical characteristics very sensitive to the environmental conditions. Graphene-based sensors have demonstrated superior sensitivities for the gas, molecular, biological and electrochemical sensing [62]-[65]. In these chemically-specific, label-free graphene sensors, chemical species adsorbed on the graphene surface may act as the n-/p-type dopants, leading to changes in transconductances of graphene field-effect devices [62]-[65] or changes in optical properties of graphene-based

plasmonic sensors [51],[66],[67]. Here, we propose, for the first time, a different sensing scheme using the $\mathcal{PT}$-symmetric graphene device in Fig. 1. We notice that for $\mathcal{PT}$-symmetric systems realized with balanced gain and loss, the bandwidth of eigenvalue bifurcation is typically quite narrow [see Fig. 5], which may be, in principle, very useful for sensing applications. In reality, due to frequency dispersion of metasurface's surface impedance, the $\mathcal{PT}$-symmetry condition cannot be fulfilled over a finite frequency interval, but only at the singular frequency point ω_0, as can be verified by the causality principle and Kramers-Kronig relations [68] (see Appendix D for details). If the device is based on graphene metasurface, the existence of $\mathcal{PT}$-symmetric/-broken transition may be very sensitive to n-/p-type surface adsorbates in graphene, which may remarkably alter graphene's dynamic conductivity σ. In this scenario, the unidirectional scattering properties of our $\mathcal{PT}$-symmetric THz system operated at the exceptional point can be chemically sensitive. In the following, we demonstrate that even a small change in carrier density of graphene due to charged impurities (e.g. doping by chemical and biological agents) may dramatically modulate scattering properties of the graphene-based $\mathcal{PT}$-symmetric system.

Figure 6(a) shows the calculated transmittance and reflectance spectra for the $\mathcal{PT}$-symmetric THz device in Fig. 5(a) ($\omega_0 / 2\pi = 1.5$ THz) before (dashed lines) and after (solid lines) the chemical doping; here we assume the n-type surface dopants lead to a small shift of quasi-Fermi level $\Delta E_{Fn} = 5$ meV ($E_{Fn} = \varepsilon_F + \Delta E_{Fn}$ and

$E_{Fp} = \varepsilon_F$). It is seen that the change in the reflectance $|r_B|^2$ can be dramatic, more than 40 dB at the exceptional point ω_0. We note that both n-type and p-type shifts may result in the same changes in scattering properties, since charged carriers in graphene obey a linear energy dispersion relation [42]. Here, we also compare the performance of this $\mathcal{PT}$-symmetric sensor with a passive plasmonic sensor consisting of an unpumped graphene metasurface.[66] This passive metasurface shares similar geometry with Fig. 1(a), but with Fermi energy E_F = 15 meV, period $a = 5.6\,\mu\text{m}$, gap size $g = 190\,\text{nm}$, and an air gap separated from a metallic ground plane by 40 μm. For a pristine graphene, such system exhibits a resonance frequency of 1.5 THz. Figure 6(b) shows the reflectance spectrum for this graphene-based plasmonic sensor in the initial condition ($\Delta E_F = 0$ meV) and after chemical doping that causes a shift in Fermi energy $\Delta E_F = 5$ meV. From Figs. 6(a) and 6(b), it is clearly seen that although a passive graphene plasmonic sensor can also be tunable through chemical doping, it shows much reduced sensitivities in comparison with a $\mathcal{PT}$-symmetric sensor. Figures 7(a) and 7(b) present the frequency of minimum $|r_B|^2$ and the magnitude of $|r_B|^2$ at 1.5 THz, as a function of the density of charged impurities n_{imp} (or ΔE_{Fn}). Here we define sensitivities as the ratio of resonance frequency shift $\Delta\omega_0 / 2\pi$ to impurity density n_{imp} for the broad-spectrum analysis [Fig. 7(a)], and as the ratio of reflectance change $\Delta |r_B|^2$ to n_{imp} for the monochromatic THz probing [Fig. 7(b)]. We find that for the monochromatic THz probing, even the light n-/p-type doping may devastate the

existence of spontaneous $\mathcal{PT}$-symmetry breaking, resulting in a dramatic change in r_B and an ultrahigh sensitivity of 4.5 dB/μm^2 (blue shadow region) that is orders of magnitude higher than the passive graphene plasmonic sensor. Further, for the broad-spectrum analysis, the $\mathcal{PT}$-symmetric sensor exhibits a high sensitivity of 1.15 GHz/μm^2 (red shadow regime), which is also significantly greater than the graphene plasmonic sensor; here these two sensitivity factors are calculated based on the fitted slopes in Fig. 7. Since the negative surface resistance of graphene metasurface modulates only the magnitude of reflection and its dispersion is relatively flat, as seen in Fig. 4, the frequency offset of reflection dip mostly depends on the kinetic inductance of doped graphene and the point where the averaged stored magnetic and electric energies are equal. At the resonance frequency $\omega_0 \approx \sqrt{L_K C_{\mathrm{ES}}}$, the net surface reactance approaches zero, and, if the surface resistance is not exactly equal to $-\mathrm{Z}_0/2$, a nonzero r_B is obtained, as shown in Fig. 5(a). We note that the separation distance between the metasurface and the metal film has no influence on the resonance frequency, as long as the surface impedance of self-resonant graphene metasurface approaches $-\mathrm{Z}_0/2$ [Eq. (2)]. On the other hand, for a passive graphene plasmonic sensor, the resonant absorption occurs when the surface reactance of metasurface cancels out the input impedance yielded by the grounded dielectric substrate $X_d = j\mathrm{Z}_0 \tan\left(k_0 d\right)$.[57] In general, the distance between the metasurface and the metallic ground is subwavelength, and, therefore, X_d can be approximately modeled as a surface inductance $L_d = \mu_0 d$ mounted in parallel to the metasurface.

In this case, if the loss is moderately low, the resonance frequency is given by $\omega_0 \approx \sqrt{C_{ES}\left(L_K + L_d\right)}$, which renders a less sensitive frequency offset when L_K is varied by chemical doping, as compared to a $\mathcal{PT}$-symmetric sensor. Figure 7 clearly demonstrates that a $\mathcal{PT}$-symmetric device, if combined with sensing functions of low-dimensional nanomaterials, can potentially outperform conventional photonic and plasmonic sensors.

V. CONCLUSIONS

We have presented a $\mathcal{PT}$-symmetric device based on the optically-pumped graphene metasurface that displays a negative surface resistance and thus amplification effect at THz frequencies. By tailoring the geometry of graphene metasurface, the gain, loss, and reactive power can be perfectly balanced in the vicinity of the exceptional point. Thanks to the sharp spectral singularities of the gain/loss-balanced $\mathcal{PT}$-symmetric system and the chemically-sensitive conductance of graphene, we have demonstrated that even a low-level chemical doping may dramatically modulate scattering properties of a graphene-based $\mathcal{PT}$-symmetric sensor. Our findings may unveil new directions and fundamentally novel effects for optically manipulating THz waves and enhancing the sensitivity of micro-/nano-sensors.

ACKNOWLEDGMENT

The authors would like to thank Dr. L. Jay Guo and Dr. Xudong Fan at University of Michigan Ann Arbor for the inspiration and fruitful discussions on $\mathcal{PT}$-symmetric sensing devices.

APPENDIX A: DETAILS ON SCATTERING PROPERTIES

When one or more two-port networks are connected in cascade, it is typically convenient to represent each junction or circuit by a 2×2 transmission (ABCD) matrix [39],[40]. The matrix which describes the complete cascade connection may be obtained simply by multiplying the matrices describing individual building-blocks. The transmission matrix $\mathbf{M}$ is defined for a two-port network in terms of the total electric and fields at the bottom side (E_b, H_b) and the top side (E_t, H_t) as:

$$\begin{pmatrix} E_b \\ H_b \end{pmatrix} = \mathbf{M} \begin{pmatrix} E_t \\ H_t \end{pmatrix} \tag{A1}$$

For the proposed PT-symmetric device in Fig. 2, the matrix can be written as:

$$\mathbf{M} = \begin{bmatrix} A & B \\ C & D \end{bmatrix} = \begin{bmatrix} 1 & 0 \\ Z_B^{-1} & 1 \end{bmatrix} \begin{bmatrix} \cos(x) & jZ\sin(x) \\ j\sin(x)/Z & \cos(x) \end{bmatrix} \begin{bmatrix} 1 & 0 \\ Z_T^{-1} & 1 \end{bmatrix} \tag{A2}$$

where the wave number and characteristic impedance of the dielectric spacer are $k=k_0/\eta$ and $Z=\eta Z_0$, $x=kd$, and $\{\eta \in \mathrm{R} : \eta \le 1\}$ for typical lossless dielectrics. Knowing the transmission matrix, one can calculate the scattering coefficients from the ABCD parameters in (A2) as:

$$\begin{aligned} r_B^- &= \frac{A + B/Z_0 - CZ_0 - D}{\Delta}, \quad t_T^- = \frac{2(AD - BC)}{\Delta}, \\ t_B^+ &= \frac{2}{\Delta}, \quad r_T^+ = \frac{-A + B/Z_0 - CZ_0 + D}{\Delta} \end{aligned} \tag{A3}$$

where $\Delta = A + B/Z_0 + CZ_0 + D.$ After some mathematical manipulations, the scattering coefficients are given by:

$$r_B^- = \frac{\left[\eta^2\left(Z_B - Z_0\right)\left(Z_T + Z_0\right) - Z_B Z_T\right]\sin(x) + jZ_0\left(Z_B + Z_T\right)\eta\cos(x)}{\left[Z_B Z_T + \eta^2\left(Z_0 + Z_B\right)\left(Z_0 + Z_T\right)\right]\sin(x) - j\left[2Z_B Z_T + Z_0\left(Z_B + Z_T\right)\right]\eta\cos(x)},$$

(A4a)

$$t_T^- = t_B^+ = t$$
$$= \frac{2\eta Z_T Z_B}{\eta\left[2Z_T Z_B + Z_0(Z_T + Z_B)\right]\cos[x] + j\left[Z_T Z_B + \eta^2\left(Z_0 + Z_B\right)\left(Z_0 + Z_T\right)\right]\sin(x)},$$

(A4b)

$$r_T^+ = \frac{\left[\eta^2\left(Z_B + Z_0\right)\left(Z_T - Z_0\right) - Z_T Z_B\right]\sin(x) + j\eta Z_0\left(Z_B + Z_T\right)\cos(x)}{\left[Z_T Z_B + \eta^2\left(Z_0 + Z_B\right)\left(Z_0 + Z_T\right)\right]\sin(x) - j\eta\left[2Z_T Z_B + Z_0\left(Z_B + Z_T\right)\right]\cos(x)},$$

(A4c)

where $\pm$ represents the forward $(+\hat{z})$ and backward $(-\hat{z})$ propagating waves. In the specific case of $\eta = 1$, $Z_T / Z_0 = -\kappa$ and $Z_B / Z_0 = \kappa$, $\{\kappa \in \mathrm{R} : \kappa \geq 0\}$, a set of transmission and reflection coefficients can be expressed as in Eq. (1). We note that there are two types of unidirectional reflectionless propagations. If $\kappa = \eta/(1+\eta)$ and $x = n\pi + \sin^{-1}\left[1/(2+2\eta)\right]$ (n is an integer), one may obtain the scattering properties as $|r_T| = |t| = 1$ and $|r_B| = 0$. On the other hand, if $\eta \leq 1/2$, $\kappa = \eta/(1-\eta)$, and $x = n\pi + \sin^{-1}\left[1/(2-2\eta)\right]$ (n is an integer), one may obtain the second type of unidirectional reflectionless properties as $|r_B| = |t| = 1$ and $|r_T| = 0$.

APPENDIX B: PHOTODOPING AND ITS REALTION TO PUMP INTENSITIES

Under equilibrium conditions, the electron density n_0 and hole density p_0 in graphene, as a function of Fermi energy E_F, can be obtained from the integration of density of states weighted by the Fermi-Dirac distribution as [51]:

$$n_0\left(E_F\right)=-\frac{2}{\pi}\left(\frac{K_{\mathrm{B}}T}{\hbar v_{\mathrm{F}}}\right)^2 Li_2\left[-e^{-qE_F/(K_{\mathrm{B}}T)}\right], \tag{B1}$$

$$p_0\left(E_F\right)=-\frac{2}{\pi}\left(\frac{K_{\mathrm{B}}T}{\hbar v_{\mathrm{F}}}\right)^2 Li_2\left[-e^{qE_F/(K_{\mathrm{B}}T)}\right], \tag{B2}$$

where the dilogarithm Li_2 is a special case of the polylogarithm $Li_n(\cdot)$ for n = 2. For a pristine graphene with $E_F = 0$, the carrier densities are obtained as:

$$n_0(0)=p_0(0)=\frac{\pi}{6}\left(\frac{k_BT}{\hbar v_F}\right)^2, \tag{B3}$$

where v_F is the Fermi velocity in graphene. The carrier densities for a n (donor)-type or p (acceptor)-type doped graphene with $\left|E_F\right| >> k_BT$, based on Eq. (B2), are given by:

$$n_0(E_F)=p_0(-E_F)=\frac{\left|E_F\right|^2}{\pi\hbar^2v_F^2}. \tag{B4}$$

Under near-infrared and visible illuminations, the excess electrons and holes are generated in pairs ($\delta n=\delta p$), and the total carrier densities become $n = n_0 + \delta n$ and $p = p_0 + \delta p$. The density of photoexcited carriers are given by:

$$\delta n=\delta p=\frac{\alpha I_{\Omega_0}\tau_r}{\hbar\Omega_0} \tag{B5}$$

, where α is the optical absorptance, I_{Ω_0} and $\hbar\Omega_0$ are the intensity and photon energy of the pump light, and τ_r is the recombination lifetime for electron-hole pairs (typically $\tau_r \sim$ ns). Under a weak optical excitation, i.e. $\varepsilon_F << K_BT$, the normalized densities of excess carriers are derived as:

$$\frac{\delta n}{n_0}=\frac{\delta p}{p_0}\approx\frac{12\ln 2}{\pi^2}\frac{\varepsilon_F}{k_{\mathrm{B}}T}. \tag{B6}$$

From Eqs. (B5) and (B6), the quasi-Fermi levels $E_{Fn}, E_{Fp}=\pm\varepsilon_F$, as a function of intensity of pump light, are given by:

$$\frac{\varepsilon_F}{k_BT}=\frac{\pi}{2\ln 2}\left(\frac{\hbar v_F}{k_BT}\right)^2\frac{\alpha I_{\Omega_0}\tau_r}{\hbar\Omega_0}. \tag{B7}$$

On the other hand, under an intense optical excitation, i.e. $\varepsilon_F>>K_BT$, the normalized densities of excess carriers are derived as:

$$\frac{\delta n}{n_0}=\frac{\delta p}{p_0}\approx\frac{6}{\pi^2}\left(\frac{\varepsilon_F}{k_{\mathrm{B}}T}\right)^2-1. \tag{B8}$$

From Eqs. (B5) and (B8), ε_F , as a function of intensity of pump light, is given by:

$$\frac{\varepsilon_F}{k_{\mathrm{B}}T}=\sqrt{\frac{\pi^2}{6}\left(1+\frac{\delta n}{n_0}\right)}\approx\sqrt{\left(\frac{\pi^2}{6}+\pi\left(\frac{\hbar v_F}{k_BT}\right)^2\frac{\tau_r\alpha I_{\Omega_0}}{\hbar\Omega_0}\right)}. \tag{B9}$$

In the near-infrared and visible ranges, $\hbar\Omega_0 >> \varepsilon_F, k_B T$ and, therefore, the optical conductivity σ, based on Eq. (4), can be expressed as:

$$\sigma(\Omega_0) = \frac{q^2}{4\hbar}\tanh\left(\frac{\hbar\Omega_0 - 2\varepsilon_F}{4k_B T}\right) \approx \frac{q^2}{4\hbar}, \tag{C10}$$

which leads to a constant optical absorption $\alpha \approx (q^2/\hbar)Z_0/4 = 2.3\%$ over a broad near-infrared and visible spectral range. For instance, assuming a pump source at $\Omega_0/2\pi$=193 THz and the recombination time $\tau_r = 1$ ns, an energy splitting of $\varepsilon_F = 15$ meV at $T = 3$ K requires the pump intensity $I_{\Omega_0} = 146$ mW/mm^2. For a larger energy splitting, for instance $\varepsilon_F = 100$ meV, the required pump intensity is increased to $I_{\Omega_0} = 6500$ mW/mm^2. These intensity are fairly reasonable at the telecommunication wavelengths.

APPENDIX C: DETAILS ON SURFACE IMPEDANCE OF GRAPHENE METASURFACE

According to impedance boundary conditions, a discontinuity on the tangential magnetic field on the metasurface is related to the induced averaged surface current by the surface impedance. Assuming a (perfectly conducting) metallic strips of zero thickness, aligned parallel to the magnetic field of the TM-polarized plane wave (corresponds to the incidence plane *y-z* with $(\mathbf{k}\times\mathbf{E})\cdot\hat{z}$=0) incident at angle θ, the equivalent surface impedance can be explicitly written as [69]:

$$Z_s^{(\mathrm{TM})} = -j\frac{Z_0}{\psi\cos\theta}\left[\ln\left[\csc\left(\frac{\pi\varphi}{2}\right)\right]+ \right.$$
$$\left. +\frac{1}{2}\frac{(1-\mathrm{B})^2\left((1-\mathrm{B}^2/4)(\mathrm{A}_+ + \mathrm{A}_-)+4\mathrm{B}^2\mathrm{A}_+\mathrm{A}_-\right)}{(1-\mathrm{B}^2/4)+\beta^2(1+\mathrm{B}^2/2-\mathrm{B}^4/8)(\mathrm{A}_+ + \mathrm{A}_-)+2\mathrm{B}^6\mathrm{A}_+\mathrm{A}_-}\right]^{-1} \quad \text{(C1)}$$

where

$$\mathrm{A}_\pm = 1/\sqrt{1\pm\frac{\psi}{2}\sin\theta-\left(\frac{\psi\cos\theta}{4}\right)^2}-1,\ \mathrm{B}=\sin\left(\frac{\pi\varphi}{2}\right), \quad \text{(C2)}$$
$$\psi = 4a/\lambda,\ \varphi = g/a,$$

a is the unit cell dimension, g is the gap size, and λ is the wavelength, respectively. Equation (C2) is valid for wavelengths and incident angles that satisfy the condition $\frac{\psi}{4}(1+\sin\theta)<1$. For a uniform plane wave normally incident to the metasurface with $\psi << 1$, Eq. (C1) reduces to a capacitive surface with impedance

$$Z_s^{(\mathrm{TM})} = -j\frac{Z_0}{\psi\ln\left[\csc\left(\frac{\pi\varphi}{2}\right)\right]} \quad \text{(C3)}$$

We note that the excitation of surface plasmon polaritons in graphene nanoribbon will also contribute to a series surface impedance as [53]-[57]:

$$Z_{\mathrm{graphene}} = \frac{1}{\sigma(1-\varphi)} = \frac{\mathrm{Re}[\sigma]-j\,\mathrm{Im}[\sigma]}{(1-\varphi)\,|\sigma|^2}. \quad \text{(C4)}$$

Therefore, the graphene-nanoribbon array can be modeled with its shunt average surface impedance, which neglects the higher order Floquet harmonics, as:

$$Z_s = Z_{\mathrm{graphene}} + Z_s^{(\mathrm{TM})}, \quad \text{(C5)}$$

Eq. (C5) can be expanded into the form in Eq. (8).

APPENDIX D: DETAILS ON RESTRICTIONS IMPOSED BY CAUSALITY

In the one-dimensional system including both absorbing and amplifying impedance surfaces [Fig. 1a], the $\mathcal{PT}$-symmetry happens when $Z_s(\omega,\mathbf{r})$ satisfies the conditions:

$$\mathrm{Re}[Z_s(\omega,\mathbf{r})] = -\mathrm{Re}[Z_s(\omega,-\mathbf{r})], \tag{D1a}$$

$$\mathrm{Im}[Z_s(\omega,\mathbf{r})] = \mathrm{Im}[Z_s(\omega,-\mathbf{r})]. \tag{D1b}$$

The surface impedance $\mathrm{Re}[Z_s(\omega,\mathbf{r})] = R_s(\omega,\mathbf{r})$ and $\mathrm{Im}[Z_s(\omega,\mathbf{r})] = X_s(\omega,\mathbf{r})$ must be causal, namely being an analytic function without poles in the upper half-plane of the complex frequency plane. Following the Kramers-Kronig relations [39], the real and imaginary parts of the surface reactance are connected by:

$$\mathrm{Re}[Z_s(\omega,\mathbf{r})] = \frac{2}{\pi}\mathrm{P}\int_0^\infty \frac{\omega'\,\mathrm{Im}[Z_s(\omega',\mathbf{r})]}{\omega'^2-\omega^2}d\omega', \tag{D2a}$$

$$\mathrm{Im}[Z_s(\omega,\mathbf{r})] = -\frac{2\omega}{\pi}\mathrm{P}\int_0^\infty \frac{\mathrm{Re}[Z_s(\omega',\mathbf{r})]}{\omega'^2-\omega^2}d\omega', \tag{D2b}$$

where integrals are taken in the sense of principal value P. Equations (D2a) and (D2b) represent that the surface reactance is internally consistent with the surface resistance, and vice versa. If $\mathcal{PT}$-symmetry condition (D1a) is satisfied for the real-part surface impedance for any real frequencies, it follows from Eqs. (D2a) and (D1b) that:

$$\mathrm{Re}[Z_s(\omega,-\mathbf{r})] = \frac{2}{\pi}\mathrm{P}\int_0^\infty \frac{\omega'\,\mathrm{Im}[Z_s(\omega',-\mathbf{r})]}{\omega'^2-\omega^2}d\omega' = \frac{2}{\pi}\mathrm{P}\int_0^\infty \frac{\omega'\,\mathrm{Im}[Z_s(\omega',\mathbf{r})]}{\omega'^2-\omega^2}d\omega' \tag{D3}$$

Now, from Eqs. (D2a) and (D3), we know that the surface reactance must satisfy the condition:

$$\int_0^\infty \frac{\omega' \,\mathrm{Im}[Z_s(\omega', \mathbf{r})]}{\omega'^2 - \omega^2} \equiv 0. \tag{D4}$$

This implies that the $\mathcal{PT}$-symmetry condition at any real frequencies can hold only when $\mathrm{Im}[Z_s(\omega, \mathbf{r})] \equiv 0$, i.e. the conjugate cancellation of inductive and capacitive reactances in the entire frequency range. For most metasurfaces that have frequency dispersions, the inductive and capacitive surface reactances can cancel each other only at the resonance frequency, as can be seen in Fig. 4. Hence, the $\mathcal{PT}$-symmetry condition cannot hold in the entire frequency range. Instead, it may exist in optical systems only at isolated frequencies.

REFERENCES

[1] C. M. Bender and S. Boettcher, Real Spectra in Non-Hermitian Hamiltonians Having PT Symmetry, *Phys. Rev. Lett*. **80**, 5243 (1998).

[2] C. M. Bender, D. C. Brody, and H. F. Jones, Complex Extension of Quantum Mechanics, *Phys. Rev. Lett*. **89**, 270401 (2002).

[3] C. M. Bender, Making Sense of Non-Hermitian Hamiltonians, *Rep. Progr. Phys*. **70**, 947 (2007).

[4] A Ruschhaupt, F Delgado and J G Muga, Physical Realization of PT-symmetric Potential Scattering in a Planar Slab Waveguide, *J. Phys. A: Math. Gen*. **38**, L171 (2005).

[5] K. G. Makris, R. El-Ganainy, and D. N. Christodoulides, Beam Dynamics in PT Symmetric Optical Lattices, *Phys. Rev. Lett*. **100**, 103904 (2008).

[6] R. El-Ganainy, K. G. Makris, D. N. Christodoulides, and Z. H. Musslimani, Theory of Coupled Optical PT-Symmetric Structures, *Opt. Lett.* **32**, 2632-2634 (2007).

[7] Y.-C. Lee, M.-H. Hsieh, S. T. Flammia, and R.-K. Lee, Local PT Symmetry Violates the No-Signaling Principle, *Phys. Rev. Lett.* **112**, 130404 (2014).

[8] A. Guo, G. J. Salamo, D. Duchesne, R. Morandotti, M. Volatier-Ravat, V. Aimez, G. A. Siviloglou, and D. N. Christodoulides, Observation of PT-Symmetry Breaking in Complex Optical Potentials, *Phys. Rev. Lett*. **103**, 093902 (2009).

[9] S. Longhi, PT -Symmetric Laser Absorber, *Phys. Rev. A* **82**, 031801(R) (2010).

[10] S. Longhi, Bloch Oscillations in Complex Crystals with PT Symmetry, *Phys. Rev. Lett*. **103**, 123601 (2009).

[11] C. E. Ruter, K. G. Makris, R. El-Ganainy, D. N. Christodoulides, M. Segev, and D. Kip, Observation of Parity-Time Symmetry in Optics, *Nat. Phys.* **6**, 192 (2010).

[12] H. Ramezani, T. Kottos, R. El-Ganainy, and D. N. Christodoulides, Unidirectional Nonlinear PT –Symmetric Optical Structures, *Phys. Rev. A* **82**, 043803 (2010).

[13] Z. Lin, H. Ramezani, T. Eichelkraut, T. Kottos, H. Cao, and D. N. Christodoulides, Unidirectional Invisibility Induced by PT-Symmetric Periodic Structures, *Phys. Rev. Lett.* **106**, 213901 (2011).

[14] L. Ge, Y. D. Chong, and A. D. Stone, Conservation Relations and Anisotropic Transmission Resonances in One-Dimensional PT -Symmetric Photonic Heterostructures, *Phys. Rev. A* **85**, 023802 (2012).

[15] Y. D. Chong, L. Ge, and A. D. Stone, PT -Symmetry Breaking and Laser-Absorber Modes in Optical Scattering Systems, *Phys. Rev. Lett*. 106, 093902 (2011).

[16] Z. Lin, J. Schindler, F. M. Ellis, and T. Kottos, Experimental Observation of the Dual Behavior of PT-Symmetric Scattering, *Phys. Rev. A* **85**, 050101(R) 2012.

[17] A. Regensburger, C. Bersch, M. A. Miri, G. Onishchukov, D. N. Christodoulides, and U. Peschel, Parity-Time Synthetic Photonic Lattices, *Nature* **488**, 167 (2012).

[18] X. Zhu, L. Feng, P. Zhang, X. Yin, and X. Zhang, One-Way Invisible Cloak Using Parity-Time Symmetric Transformation Optics, *Opt. Lett.* **38**, 2821 (2013).

[19] M. Kang, F. Liu, and J. Li, Effective Spontaneous PT-Symmetry Breaking in Hybridized Metamaterials, *Phys. Rev. A* **87**, 053824 (2013).

[20] N. Bender, S. Factor, J. D. Bodyfelt, H. Ramezani, D. N. Christodoulides, F. M. Ellis, and T. Kottos, Observation of Asymmetric Transport in Structures with Active Nonlinearities, *Phys. Rev. Lett*. **110**, 234101 (2013).

[21] G. Castaldi, S. Savoia, V. Galdi, A. Alù, and N. Engeta, PT Metamaterials via Complex-Coordinate Transformation Optics, *Phys. Rev. Lett.* **110**, 173901 (2013).

[22] S. Savoia, G. Castaldi, V. Galdi, A. Alù, and N. Engeta, Tunneling of Obliquely-Incident Waves through PT-Symmetric Epsilon-Near-Zero Bi-Layers, *Phys. Rev. B* **89**, 085105 (2014).

[23] R. Fleury, D. L. Sounas, and A. Alù, Negative Refraction and Planar Focusing Based on Parity-Time Symmetric Metasurfaces, *Phys. Rev. Lett.* **113**, 023903 (2014).

[24] S. Savoia, G. Castaldi, V. Galdi, A. Alù, and N. Engheta, PT-Symmetry-Induced Wave Confinement and Guiding in □-Near-Zero Metamaterials, *Phys. Rev. B* **91**, 115114 (2015).

[25] B. Peng, Ş. K. Özdemir, F. Lei, F. Monifi, M. Gianfreda, G. L. Long, S. Fan, F. Nori, C. M. Bender, and L. Yang, Parity-Time-Symmetric Whispering-Gallery Microcavities, *Nat. Phys*. **10**, 394 (2014).

[26] C. Yidong, Nonlinear Optics: Asymmetry from Symmetry, *Nat. Phys*. **10**, 336 (2014).

[27] H. Alaeian and J. A. Dionne, Non-Hermitian Nanophotonic and Plasmonic Waveguides, *Phys. Rev. B* **89**, 075136 (2014).

[28] X. Zhu, H. Ramezani, C. Shi, J. Zhu, and X. Zhang, PT-Symmetric Acoustics, *Phys. Rev. X* **4**, 031042 (2014).

[29] R. Fleury, D. Sounas, and A. Alù, An Invisible Acoustic Sensor Based On Parity-Time Symmetry, *Nat. Commun*. **6**, 5905 (2015).

[30] A. Lupu, H. Benisty, and A. Degiron, Switching Using PT Symmetry in Plasmonic Systems: Positive Role of the Losses, *Opt. Express* **21**, 21651-21668 (2013).

[31] A. A. Sukhorukov, Z. Xu, and Y. S. Kivshar, Nonlinear Suppression of Time Reversal in PT-Symmetric Optical Coupler, *Phys. Rev. A* **82**, 043818 (2010).

[32] V. Ryzhii, M. Ryzhii, and T. Otsuji, Negative Dynamic Conductivity of Graphene with Optical Pumping, *J. Appl. Phys*. **101**, 083114 (2007).

[33] V. Ryzhii, M. Ryzhii, V. Mitin, and T. Otsuji, Toward the Creation of Terahertz Graphene Injection Laser, *J. Appl. Phys*. **110**, 094503 (2011).

[34] T. Watanabe, T. Fukushima, Y. Yabe, S. A. Boubanga Tombet, A. Satou, A. A. Dubinov, V. Ya Aleshkin, V. Mitin, V. Ryzhii, T. Otsuji, Gain Enhancement Effect of Surface Plasmon Polaritons on Terahertz Stimulated Emission in Optically Pumped Monolayer Graphene, *New J. Phys.* **15**, 075003 (2013).

[35] T. Otsuji, T. Watanabe, A. A. Boubanga Tombet, A. Satou, W. M. Knap, V. V. Popov, M. Ryzhii, and V. Ryzhii, Emission and Detection of Terahertz Radiation Using Two-Dimensional Electrons in III–V Semiconductors and Graphene, *IEEE Trans. THz Sci. Technol*. **3**, 63-71 (2013).

[36] D. Svintsov, V. Ryzhii, A. Satou, T. Otsuji, and V. Vyurkov, Carrier-Carrier Scattering and Negative Dynamic Conductivity in Pumped Graphene, *Opt. Express* **22**, 19873 (2014).

[37] P. Weis, J. L. Garcia-Pomar, and M. Rahm, Towards Loss Compensated and Lasing Terahertz Metamaterials Based on Optically Pumped Graphene, *Opt. Express* **22**, 8473 (2014).

[38] Y. S. Lee, *Principle of Terahertz Science and Technology*, Springer, New York (2009).

[39] S. Tretyakov, *Analytical modeling in applied electromagnetics*, Artech House, London (2003).

[40] D. M. Pozar, *Microwave Engineering*, Wiley, New York (2011).

[41] F. Bonaccorso, Z. Sun, T. Hanson, A. C. Ferrari, Graphene Photonics and Optoelectronics, *Nat. Photon*. **4**, 611-622 (2010).

[42] P. Avouris, Graphene: Electronic and Photonic Properties and Devices, *Nano Lett*. **10**, 4285-4294 (2010).

[43] T. Low, and P. Avouris, Graphene Plasmonics for Terahertz to Mid-infrared Applications, *ACS Nano* **8**, 1086-1101 (2014).

[44] H. Yan, T. Low, W. Zhu, Y. Wu, M. Freitag, X. Li, F. Guinea, and P. Avouris, and F. Xia, Damping Pathways of Mid-infrared Plasmons in Graphene Nanostructures, *Nat. Photon.* **7**, 394-399 (2013).

[45] L. A. Falkovsky, and S. S. Pershoguba, Optical Far-Infrared Properties of a Graphene Monolayer and Multilayer, *Phys. Rev. B* 76, 153410 (2007).

[46] L. A. Falkovsky and A. A. Varlamov, Space-time dispersion of graphene conductivity, *Euro. Phys. J. B* **56**, 281-284 (2007).

[47] G. W. Hanson, Dyadic Green's Functions and Guided Surface Waves for a Surface Conductivity Model of Graphene, *J. Appl. Phys.* **103**, 064302 (2008).

[48] P. Y. Chen, and A. Alù, Atomically Thin Surface Cloak Using Graphene Monolayers, *ACS Nano* **5**, 5855-5863 (2011).

[49] P. Y. Chen, M. Farhat, A. N. Askarpour, M. Tymchenko, and A. Alù, Infrared Beam-Steering Using Acoustically Modulated Surface Plasmons Over a Graphene Monolayer, *J. Opt.* **16**, 094008 (2014).

[50] P. Y. Chen, C. Argyropoulos, and A. Alù, Terahertz Antenna Phase Shifters Using Integrally-Gated Graphene Transmission-Lines, *IEEE Trans. Antenna Propagat.* **61**, 1528-1537 (2013).

[51] P. Y. Chen, H. Huang, D. Akinwande, and A. Alù, Graphene-Based Plasmonic Platform for Reconfigurable Terahertz Nanodevices, *ACS Photon.* **1**, 647-654 (2014).

[52] I. Gierz, J. C. Petersen, M. Mitrano, C. Cacho, E. Turcu, E. Springate, A. Sthr, A. Khler, U. Starke, and A. Cavalleri, Snapshots of Non-equilibrium Dirac Carrier Distributions in Graphene, *Nat. Mater***. 12**, 1119–1124 (2013).

[53] Y. R. Padooru, A. B. Yakovlev, C. S. R. Kaipa, G. W. Hanson, F. Medina, and F. Mesa, Dual Capacitive-Inductive Nature of Periodic Graphene Patches: Transmission Characteristics at Low-Terahertz Frequencies, *Phys. Rev. B* **87**, 115401 (2013).

[54] A. Forouzmand, and A. B. Yakovlev, Electromagnetic Cloaking of a Finite Conducting Wedge With a Nanostructured Graphene Metasurface, *IEEE Trans. Antenna Propagat.* **63**, 2191-2202 (2015).

[55] P. Y. Chen, and A. Alù, Terahertz Metamaterial Devices Based on Graphene Nanostructures, *IEEE Trans. Terahertz Sci. Technol.* **3**, 748-756 (2013).

[56] P. Y. Chen, J. Soric, Y. R. Padooru, H. M. Bernety, A. B. Yakovlev, A. Alù, Nanostructured Graphene Metasurface for Tunable Terahertz Cloaking, *New J. Phys.* **15**, 123029 (2013).

[57] P. Y. Chen, M. Farhat, and H. Bağcı, Graphene Metascreen for Designing Compact Infrared Absorbers with Enhanced Bandwidth, *Nanotechnol*. **26**, 164002 (2015).

[58] O. Luukkonen, F. Costa, C. R. Simovski, A. Monorchio, and S. A. Tretyakov, "A Thin Electromagnetic Absorber for Wide Incidence Angles and Both Polarizations, *IEEE Trans. Antenna Propagat.* **57**, 3119-3125 (2009).

[59] Y. R. Padooru, A. B. Yakovlev, P. Y. Chen, and A. Alù, Line-Source Excitation of Realistic Conformal Metasurface Cloaks, *J. Appl. Phys.* **112**, 104902 (2012).

[60] Y. R. Padooru, A. B. Yakovlev, P. Y. Chen, and A. Alù, Analytical Modeling of Conformal Mantle Cloaks for Cylindrical Objects Using Sub-Wavelength Printed and Slotted Arrays, *J. Appl. Phys*. **112**, 034907 (2012).

[61] M. Lawrence, N. Xu, X. Zhang, L. Cong, J. Han, W. Zhang, and S. Zhang, Manifestation of PT Symmetry Breaking in Polarization Space with Terahertz Metasurfaces, *Phys. Rev. Lett*. **113**, 093901 (2014).

[62] F. Schedin, A. K. Geim, S. V. Morozov, E. W. Hill, P. Blake, M. I. Katsnelson, and K. S. Novoselov, Detection of Individual Gas Molecules Adsorbed on Graphene. *Nat. Mater*. **6**, 652–655 (2007).

[63] Y. Ohno, K. Maehashi, Y. Yamashiro, and K. Matsumoto, Electrolyte-Gated Graphene Field-Effect Transistors for Detecting pH and Protein Adsorption, *Nano Lett.* **9**, 3318-3322 (2009).

[64] M. Lafkioti, B. Krauss, T. Lohmann, U. Zschieschang, H. Klauk, K. V. Klitzing, J. H. Smet, Graphene on a Hydrophobic Substrate: Doping Reduction and Hysteresis Suppression under Ambient Conditions. *Nano Lett*. **10**, 1149–1153 (2010).

[65] Y. Dan, Y. Lu, N. J. Kybert, Z. Luo, and A. T. C. Johnson, Intrinsic Response of Graphene Vapor Sensors, *Nano Lett*. **9**, 1472-1475 (2009).

[66] D. Rodrigo, O. Limaj, D. Janner, D. Etezadi, F. J. García de Abajo, V. Pruneri, and H. Altug, Mid-Infrared Plasmonic Biosensing with Graphene, *Science* **349**, 165-168 (2015).

[67] Y. Zhao, X. Hu, G. Chen, X. Zhang, Z. Tan, J. Chen, R. S. Ruoff, Y. Zhu, and Y. Lu, Infrared Biosensors Based on Graphene Plasmonics: Modeling. *Phys. Chem. Chem. Phys*. **15**, 17118-17125 (2013).

[68] A. A. Zyablovsky, A. P. Vinogradov, A. V. Dorofeenko, A. A. Pukhov, and A. A. Lisyansky, Causality and Phase Transitions in PT-Symmetric Optical Systems, *Phys. Rev. A* **89**, 033808 (2014).

[69] N., Marcuvitz, *Waveguide Handbook*, McGraw-Hill, New York (1951)

FIGURES

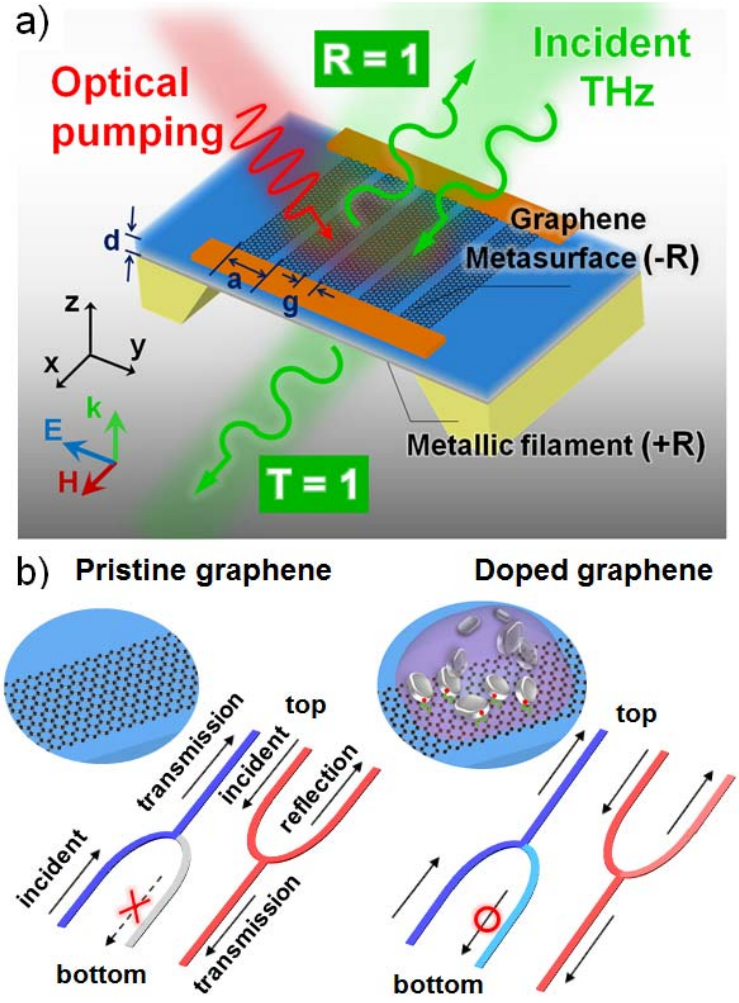

Figure 1 (a) Schematic integration of a $\mathcal{PT}$-symmetric terahertz (THz) system consisting of an active graphene metasurface and an absorbing metallic sheet. (b) Illustration of transmission and reflection of THz waves incident from the bottom (outlined as blue) and top (outlined as red) of a graphene-based $\mathcal{PT}$-symmetric sensor, before (left) and after (right) being chemically doped.

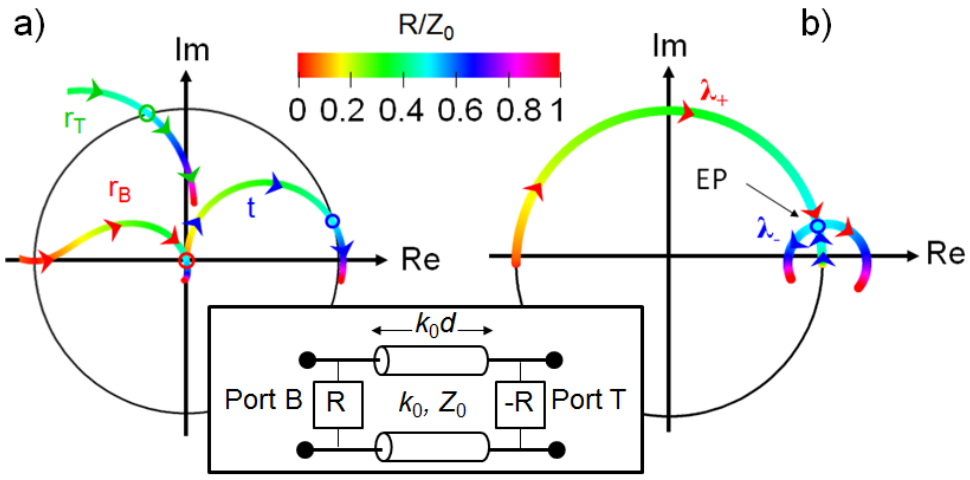

Figure 2 (a) Scattering parameters (r_T, r_B, and t) and (b) eigenvalues as a function of the R/Z_0 for the $\mathcal{PT}$-symmetric THz system in Fig. 1(a) with $k_0 d = \sin^{-1}(1/4)$; the arrows indicate the evolution of scattering parameters and eigenvalues with increasing the value of R. The inset presents the corresponding two-port transmission-line model, comprising an optically-pumped graphene metasurface with surface resistance $-R$ and a resistive sheet with surface resistance $+R$, separated by a transmission-line segment with physical length d, wave number k_0, and characteristic impedance Z_0.

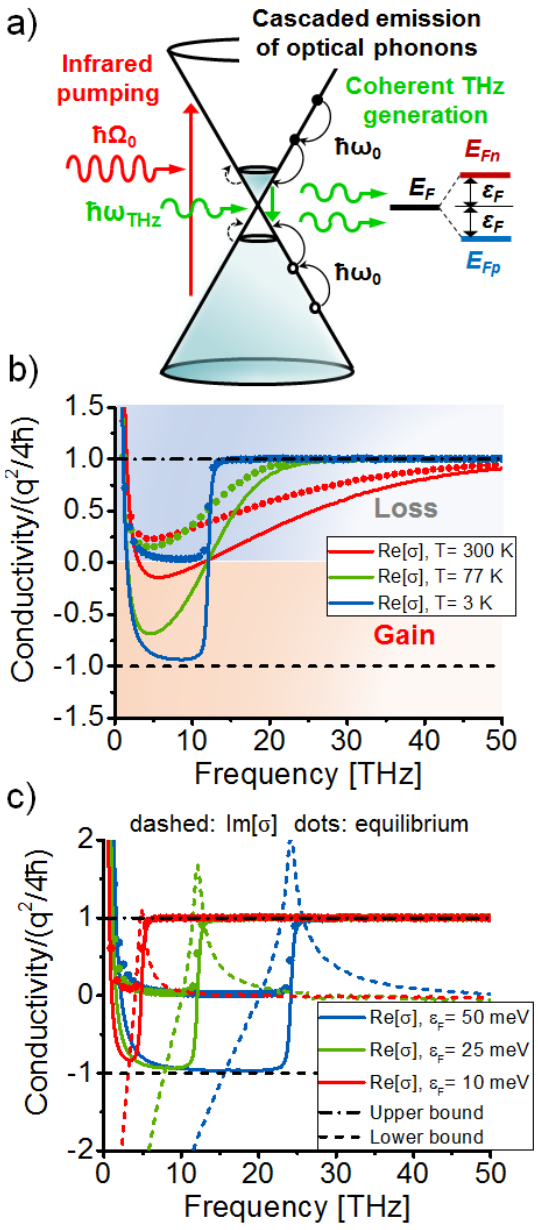

Figure 3 (a) Schematics of THz lasing in a pristine graphene (E_F = 0 eV) triggered by the optical pumping. (b) Frequency dispersion of the real conductivity Re[σ] for a pristine graphene before (dots) and after (solid lines) the optical pumping, under different temperatures. (c) Frequency dispersion of real (solid lines) and imaginary (dashed lines) conductivity for a pristine graphene photoexcited to different quasi-Fermi energies at low temperature (T = 3 K).

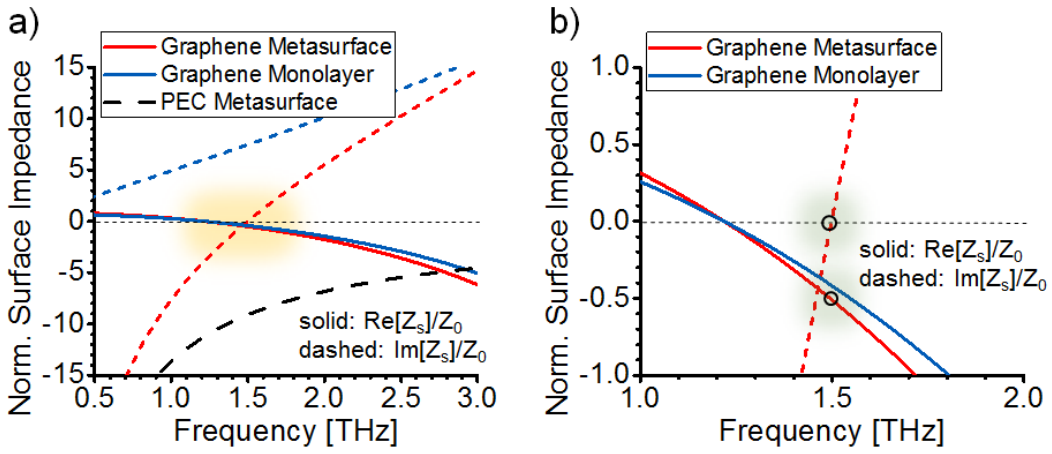

Figure 4 (a) Normalized surface impedance (R_s/Z_0) against frequency for a graphene metasurface with $\varepsilon_F = 15$ meV (red line), a graphene monolayer with $E_F = 15$ meV (blue line), and a metasurface (black line) made of perfect electric conductor (PEC). The solid and dashed line represent the real and imaginary parts of surface impedance, respectively. For a PEC metasurface, the surface resistance is zero. (b) is the room-in view of (a) around 1.5 THz.

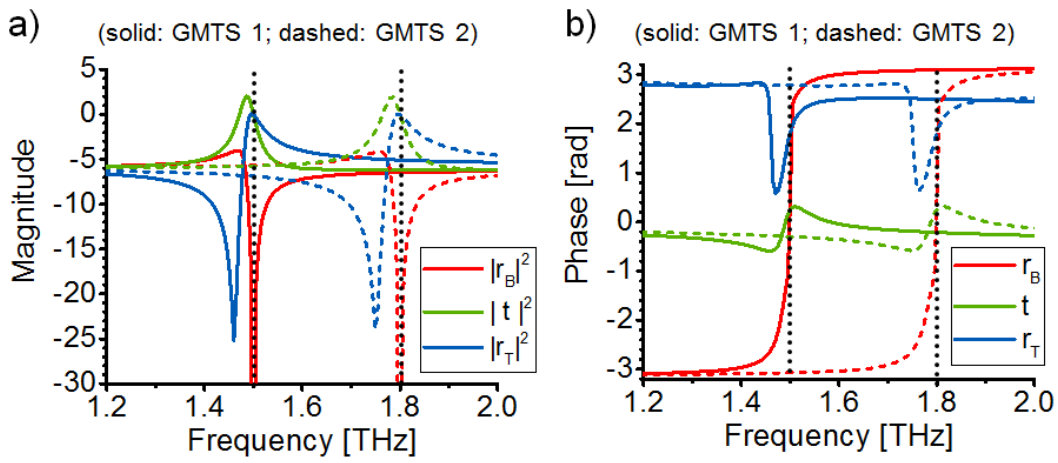

Figure 5 (a) Magnitude of reflectances ($|r_B^2|$ and $|r_T^2|$) and transmittance ($|t^2|$) against frequency for a $\mathcal{PT}$-symmetric THz device based on the photoexcited graphene metasurface. Graphene metasurface 1 (GMTS 1) [Fig. 4] and graphene metasurface 2 (GMTS 2) are designed to have the exceptional point at 1.5 THz and 1.8 THz, respectively. (b) is similar to (b), but for phase variations in the frequency response.

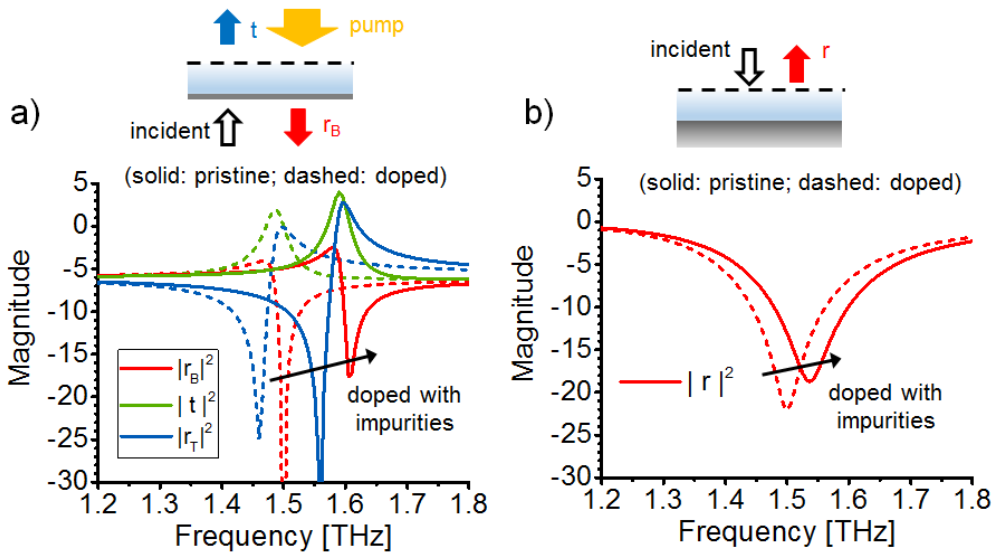

Figure 6 (a) Magnitude of scattering parameters against frequency for a graphene-based $\mathcal{PT}$-symmetric sensor before and after being chemically doped ($\varepsilon_F = 0\,\text{meV} \rightarrow \varepsilon_F = 5\,\text{meV}$). (b) is similar to (a), but for a plasmonic sensor based on graphene metasurface before and after being doped ($\varepsilon_F = 0\,\text{meV} \rightarrow \varepsilon_F = 5\,\text{meV}$).

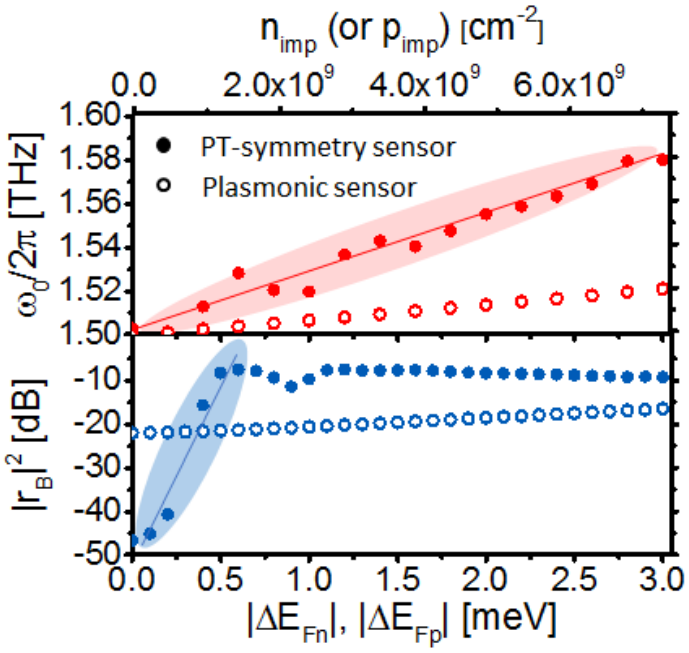

Figure 7 Frequency of r_B dip (top) and the value of $|r_B^2|$ at the exceptional point (1.5THz) (bottom) as a function of the dopant concentration for the graphene-based $\mathcal{PT}$-symmetric sensor [Fig. 6(a)]. Results for the passive, graphene-based plasmonic sensor [Fig. 6(b)] are also presented for comparisons.